FISEVIER

Contents lists available at ScienceDirect

Materials Science & Engineering A

journal homepage: www.elsevier.com/locate/msea



A multiscale comparison of stochastic open-cell aluminum foam produced via conventional and additive-manufacturing routes



Kristoffer E. Matheson^a, Kory K. Cross^a, Matthew M. Nowell^b, Ashley D. Spear^{a,*}

- ^a Department of Mechanical Engineering, University of Utah, Salt Lake City, UT, USA
- ^b AMETEK Materials Analysis Division, Draper, UT, USA

ARTICLE INFO

Keywords: Casting Rapid solidification Mechanical characterization EBSD Tomography Cellular materials

ABSTRACT

With the exciting potential of additive manufacturing of metals to produce geometrically complex structures come many unknowns and uncertainties regarding the process-microstructure-property relationships of the additively manufactured (AM) parts, especially in comparison to their conventionally manufactured counterparts. This work attempts to elucidate some key differences between AM and cast parts by conducting a multiscale comparison of samples that are intended to be identical, except for the route by which each was manufactured. The samples of interest are open-cell foams of an Al-Mg-Si alloy (Al 6061). The baseline open-cell foam is conventionally produced via investment casting. Copies are produced using laser powder bed fusion. Full-field deformation is characterized under compressive loading using in-situ X-ray computed tomography. The foams are compared in terms of global load versus displacement response, local failure mechanisms, and characteristics of the grain structure.

1. Introduction

Open-cell metallic foams are a class of structural-material systems that comprise a network of interconnected metallic ligaments, resulting in a hierarchical structure [1] – viz., the component scale of the engineered part, the topological scale of the foam, and the grain scale of individual ligaments or struts. The topology of open-cell foams can range from ordered (as in lattices) to stochastic. These low-density, hierarchical, structural-material systems have been recognized as being multifunctional [2,3]. For example, in addition to serving as lightweight, load-bearing structures, open-cell metallic foams have the potential to serve concurrently as electrodes for energy-storage devices [4], as hosts for newly generated bone and blood vessels in biomedical implants [5], or as impact absorbers and noise insulators for advanced high-speed ground transportation [3], to name a few.

There has been a considerable amount of work done to investigate and describe various manufacturing techniques to produce both openand closed-cell metallic foams [6–10]. Fig. 1 provides a partial taxonomy of the primary manufacturing routes used to produce such foams, also called cellular metals. The work presented herein focuses on stochastic open-cell foams, where investment casting (the left-most route shown in Fig. 1) is considered to be the conventional manufacturing route of interest. As shown in Fig. 1, one method of investment casting involves the production of a sacrificial polymer template

[10]. The template is then used to create a mold for casting by embedding the template in a ceramic slurry, allowing the ceramic to harden, and removing the sacrificial template by heating to temperatures above the vaporization temperature of the polymer. Molten metal is then cast using the ceramic mold. After solidification, the ceramic mold is removed, and the open-cell metal foam remains. The reader is referred to work by Ashby et al. [8] for more details regarding this and other processes for producing cellular metals.

More recently, additive manufacturing has been considered as an alternative method for producing cellular metal structures [12–20]. In general, additive manufacturing involves the creation of a structure through layer-by-layer addition of material. The geometry of the desired structure is provided via a CAD model. The software of the manufacturing system virtually slices the CAD model, and the sliced images provide the instructions to build the part through a layer-by-layer process.

For metals, in particular, additive manufacturing can be accomplished using a number of different types of systems, which include powder bed, powder feed, and wire feed systems (see review articles by Gu et al. [21] and Frazier [22]). Further, each system can vary according to its energy source. For example, in the powder bed systems, two primary energy sources for melting the powder include electron beam and laser beam. As Frazier points out [22], the advantages of the powder bed system over the powder feed or wire feed systems include

^{*} Correspondence to: University of Utah, 1550 Kennecott Building, Salt Lake City, UT 84112, USA. E-mail address: ashley.spear@utah.edu (A.D. Spear).

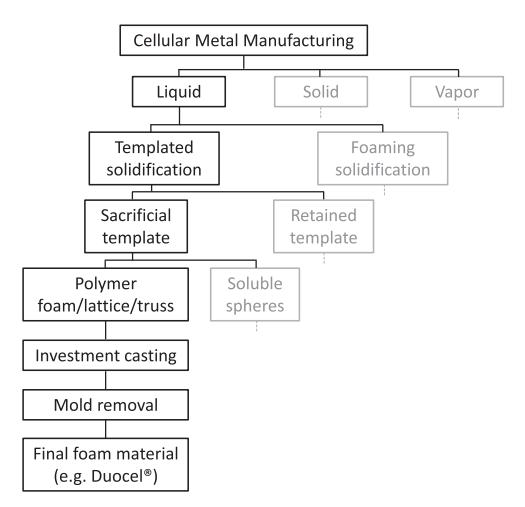


Fig. 1. Partial taxonomy of manufacturing routes for producing metallic foams (modified from [10.11]).

ability to maintain relatively tight dimensional control with relatively high resolution and ability to create complex internal passages. For these reasons, the powder bed systems are particularly well suited for creating complex and intricate geometries, like open-cell metal foams.

A number of researchers have investigated metallic lattice structures produced using powder bed systems. For example, Gorny et al. [12] investigated the local deformation and failure mechanisms in Ti-6Al-4V lattice structures produced using selective laser melting. In that work, digital image correlation was used to correlate regions of local strain concentration with the plane of final failure. Another important finding from that work was that the heat treatment following the build process served to increase ductility, and therefore energy absorption, for the lattice structure. Other studies of the mechanical response of AM lattice structures involve 316L stainless steel produced using selective laser melting [13] and titanium alloys produced using electron beam melting (EBM) [14,15].

Murr and colleagues have utilized EBM to produce both reticulated (lattice) and stochastic foam structures using such materials as titanium [16,17], copper [18], and cobalt-base [19] alloys. They have successfully demonstrated the ability to utilize X-ray computed tomography (CT) to generate the requisite CAD models to produce complex foam structures using EBM. In a review article by Murr et al. [20], the authors point to the tremendous potential of metal additive manufacturing to enable design strategies for biomedical implants.

To the authors' knowledge, there has not been a direct comparison carried out between an open-cell metal foam produced by conventional manufacturing (e.g. investment casting) and "copies" produced via additive manufacturing of the same alloy. To that end, the objectives of this manuscript are to: 1) present a method for producing copies of a conventionally manufactured, stochastic, open-cell metal foam through the use of laser powder-bed fusion (PBF), and 2) present results on the comparison among the AM copies and the conventionally manufactured foam of the same alloy.

2. Materials and methods

2.1. Materials and sample preparation

The conventional method by which the open-cell foams are produced is investment casting, which is considered to be the baseline manufacturing method in this study. The investment-cast aluminum foam used in this study has a base alloy of 6061 (subjected to a T6 post-

process heat treatment) with a reported density of 10.5% and five pores per inch (5 ppi). AM copies of the foam were created in an effort to replicate the foam geometry with the same metallic alloy of the baseline foam to enable microstructural and mechanical comparison.

As a proof-of-concept, two cylindrical geometries were bored out of the bulk investment-cast foam using electrical discharge machining. One geometry (10.0 mm diameter and 5.7 mm length, nominal) was used for characterization and comparison of grain structure, and the other (10.0 mm diameter and 18.3 mm length, nominal) was used for in-situ characterization and comparison of the crushing response. After machining, the cylindrical samples were imaged using a Varian BIR 150/130 X-ray CT imaging system (14 μm voxel spacing). For each cylindrical sample of aluminum foam, the corresponding stack of tomograms was segmented and reconstructed in Avizo* to generate an STL file of the full volume.

The STL files were then used to create copies of each cylindrical sample of foam using laser PBF. To ensure a valid comparison between foams, care was taken to obtain the same powder alloy as the alloy used in the commercially available investment-cast foam. The powder alloy was produced by Valimet, Inc., and has a special designation of AM 6061, which was certified to have spherical particles with average diameter of $34.22 \, \mu m$ [24]. The chemical composition for the AM 6061 powder is provided in Table 1.

The AM foam samples were produced using a Concept Laser M-Lab R laser PBF system. The default processing parameters for CL 31Al [25], which is Concept Laser's aluminum powder, were used. All of the samples were produced during the same build using virgin powder. One copy of the smaller sample and two copies of the larger sample (denoted Copy A and Copy B) were produced. Following the build process, all of the samples were subjected to the default heat treatment specified in Concept Laser's datasheet for stress relieving aluminum [25]. The samples were heated to 240 °C over one hour and then maintained at temperature for six hours. The samples were then allowed to cool to $100\ ^{\circ}$ C in oven. Finally, the samples were allowed to cool down in ambient atmosphere.

2.2. Grain-scale characterization

To enable grain-scale characterization and comparison, the foams had to be carefully prepared and polished without damaging the individual ligaments, or struts. To accomplish this, each of the smaller foam samples was set in a poly(methyl methacrylate) resin, or acrylic, which protected the ligaments from deforming during polishing. A quickset acrylic powder and liquid solution was used. The excess acrylic resin was sanded away and shaped using 180 grit (80 µm) silicon carbide paper. Each sample was then polished to a 0.05 μm RMS roughness rating through a series of polishing steps using an Allied Techprep 10-1000 mechanical polisher. Each sample was polished gradually using a series of polishing papers while ensuring the scratches from the previous paper were completely removed before moving on to the next paper. The first set of polishing paper used was silicon carbide and the order of polishing was 180 grit (80 µm), 320 grit (35 µm), 600 grit (15 µm). Diamond lapping film was then used with an order of 12, 9, and 3 µm. Finally alumina suspension was used with an order of 1, 0.3, and 0.05 μm. Upon completing mechanical polishing, a Fischione Model 1060 SEM Mill was used at 4.0 kV operating voltage and incident beam angle of 3° for 1.5 h to provide the final polish to the samples.

After polishing the samples, electron backscatter diffraction (EBSD) data were collected to make comparisons of grain structure resulting from the two manufacturing processes. For each of the polished samples, an entire ligament cross section was analyzed using a beam step size of 2.5 μm and 3.0 μm for the AM and investment-cast foams, respectively.

¹ Selective laser melting (SLM) was termed by ASTM in 2012 to be a "powder bed fusion" process [23].

Table 1 Chemical composition of 6061 powder provided by Valimet, Inc. (wt%) [24].

Al	Mg	Si	Cu	Fe	Cr	Mn	Ti	Zn
Bal.	0.86	0.59	0.24	0.18	0.07	0.02	0.01	< 0.01

2.3. In-situ mechanical testing

To monitor the full-field deformation of the aluminum foam during crushing, a specialized in-situ load frame was recently developed by the authors to enable collection of X-ray CT data incrementally during mechanical loading. The load frame is compatible with the Varian BIR 150/130 X-ray CT imaging system, has a low attenuation of X-rays, provides a 360° view of the sample while in the load frame, and maintains clean wire management that prevents any wires from obstructing the X-rays during scanning. Fig. 2 shows the chamber of the Xray CT imaging system along with the mechanical load frame used during in-situ testing. A captive linear stepper motor applies force (or displacement) to the lower stage of the load frame. A rigid polycarbonate tube holds the upper mount in place and prevents upward displacement of the sample as force (displacement) is applied. The specimen is held in place by two transparent polycarbonate caps, which maintain axially symmetric load and keep the foam centered about the vertical axis to facilitate tracking the field of view.

The 18.3 mm-long foam samples (one investment cast and two produced by laser PBF) were loaded in displacement control to a total displacement of 12 mm, or approximately 66% of the initial height. X-ray CT scan images were collected every 2 mm of displacement, during which the displacement was held constant.

The X-ray CT scan images from the undeformed configuration were used to calculate the precise material density for each of the compressive foam samples. Specifically, the number of pixels corresponding to solid material were quantified in each stack of X-ray CT images, which was then multiplied by the voxel size to obtain the volume of solid. The volume of solid was then divided by the nominal cylindrical volume (10.0 mm diameter, 18.3 mm length). For the volume of foam considered, the investment-cast foam had a calculated density of 12.5%. Copy A and Copy B of the laser PBF foam samples had calculated densities of 13.6% and 13.9%, respectively.

3. Results

Optical micrographs are shown in Fig. 3 for a polished cross section of the investment-cast foam and the same cross section from a copy produced via laser PBF. The inverse pole figure maps in the inset images in Fig. 3 provide a comparison of the grain structure between the investment-cast and AM foams for the same ligament in the cross section shown.

The global mechanical response of the three foam samples is plotted in terms of both force versus displacement and effective stress versus effective strain in Fig. 4. The force (F) versus displacement (d) were converted to effective stress (F/A_{eff}) versus effective strain (d/L_0) for each foam sample using the nominal, undeformed cross sectional area (10.0 mm diameter) and original length (18.3 mm), respectively. Similar to work done by Gorny et al. [12], the data collected for this experiment is sufficient not only to characterize the compressive load behavior up to the point of initial failure, but also to characterize the subsequent ability to regain load carrying capacity and thereby absorb additional energy. The initial failure in both of the AM foam copies occurred at approximately 200 N and between 0.85 and 0.9 mm of global displacement. At that point, the load-carrying capacity of Copy B dropped significantly. Copy A was able to quickly regain capacity and carried up to 350 N of load at 1.7 mm of applied displacement, at which point it experienced failure again, as indicated by the load drop. The investment-cast foam carried approximately 335 N of force before its initial failure, which occurred at 0.85 mm of global displacement. For all three foams, the initial maximum load level was not achieved again until 7-8 mm of applied displacement, at which point the foams were able to regain load-carrying capacity.

Animations of the foam crushing, alongside the corresponding force versus displacement curve, are provided for each of the three foams in the online version of this article. To generate the animations, snapshots were taken of each foam reconstruction using Avizo® and then arranged in order of increasing displacement. These were then used to generate the animations that show the progression of compression to help visualize the global foam response during mechanical testing.

The X-ray CT reconstructions for each of the three foam samples were visually inspected in ParaView to observe and classify the behavior of each individual ligament as the compression progressed. Ligaments were classified into one of four categories: those that demonstrated brittle fracture with little plastic deformation, those that exhibited only plastic collapse (such as buckling), those that

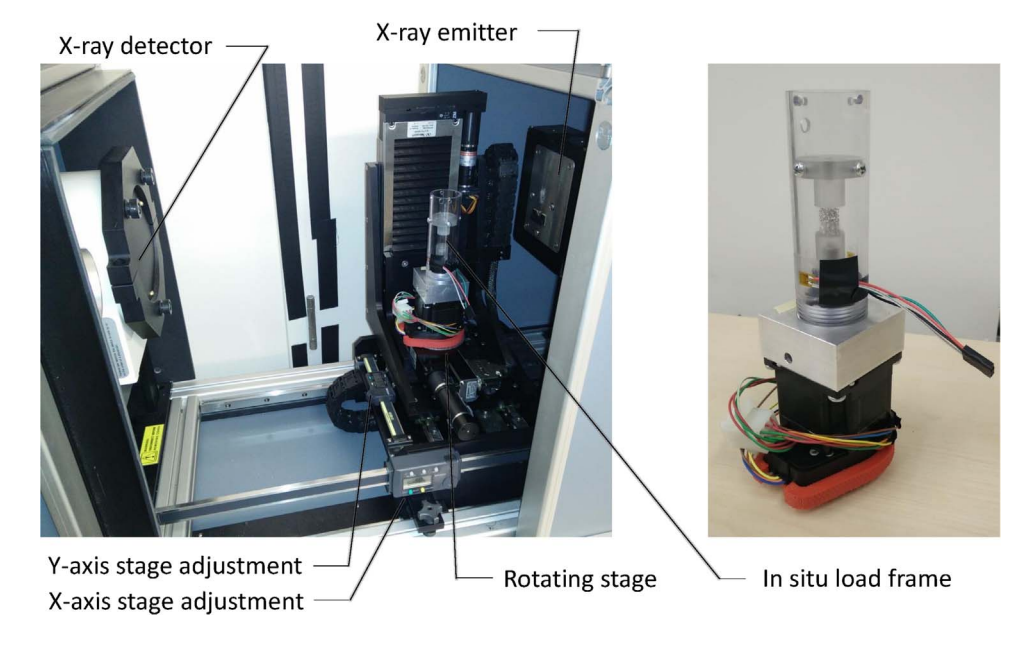


Fig. 2. Left: Chamber of Varian BIR 150/130 X-ray computed tomography imaging system with mechanical load frame in place. Right: Mechanical load frame used during in-situ imaging.

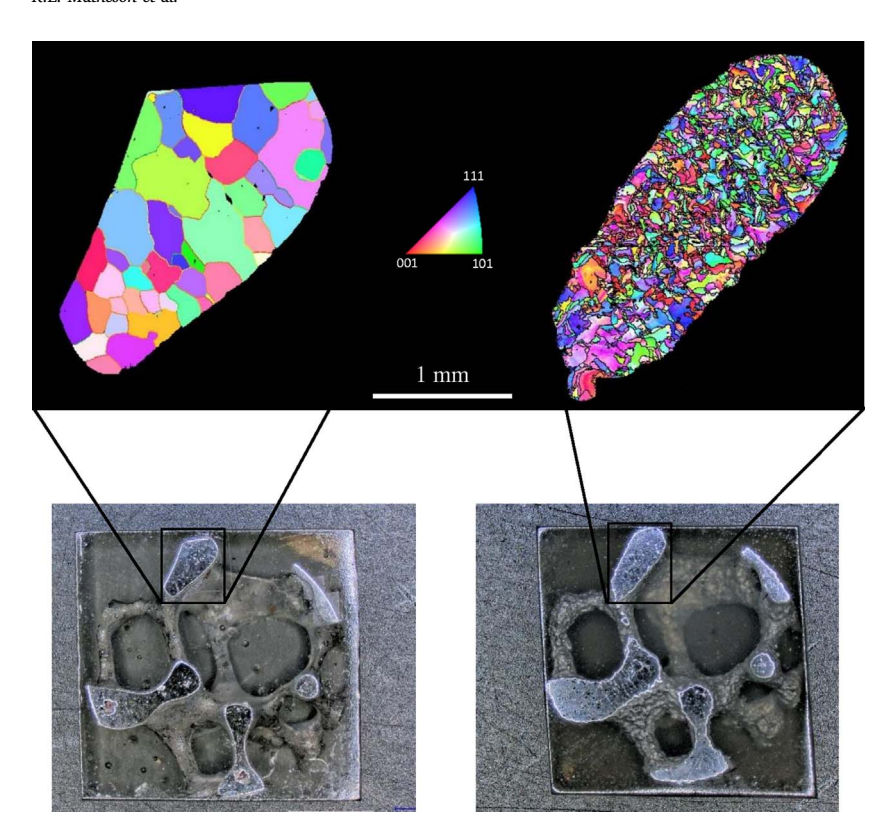


Fig. 3. Grain-scale comparison of polished foam samples, each with nominal diameter of 10.0 mm. Left: conventionally manufactured. Right: additively manufactured.

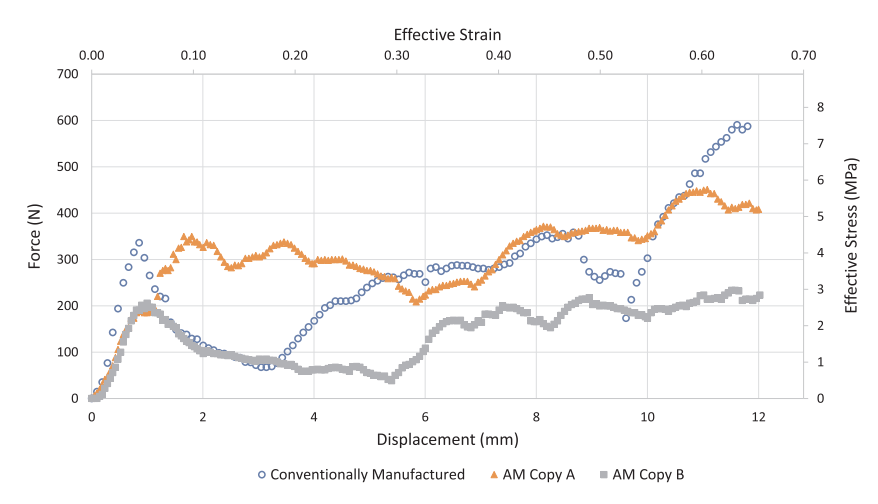
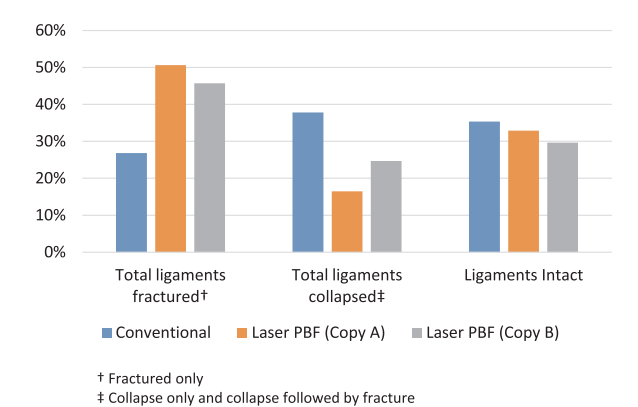


Fig. 4. Compressive response for all three foam samples.

 $\begin{tabular}{ll} \textbf{Table 2} \\ \textbf{Number of ligaments fractured, collapsed, collapsed then fractured, or intact for each foam.} \end{tabular}$

	Conventional foam	Copy A	Copy B
Fractured only	22	40	37
Collapsed only	24	7	14
Collapsed then fractured	7	6	6
Ligaments intact	29	26	24
Total ligaments	82	79	81

experienced a significant amount of plastic deformation before eventually fracturing, and those that remained intact or mostly intact. These results are presented in Table 2. Note that while the total number of ligaments in the two AM foam copies varied slightly from the original foam due to discrepancies caused by the laser PBF manufacturing process, the original foam topology was reproduced relatively well in each copy. The graph in Fig. 5 presents the total number of ligaments to



 $\textbf{Fig. 5.} \ \ \textbf{Percentage of ligaments fractured, collapsed, or intact based on total number of ligaments in each foam.}$

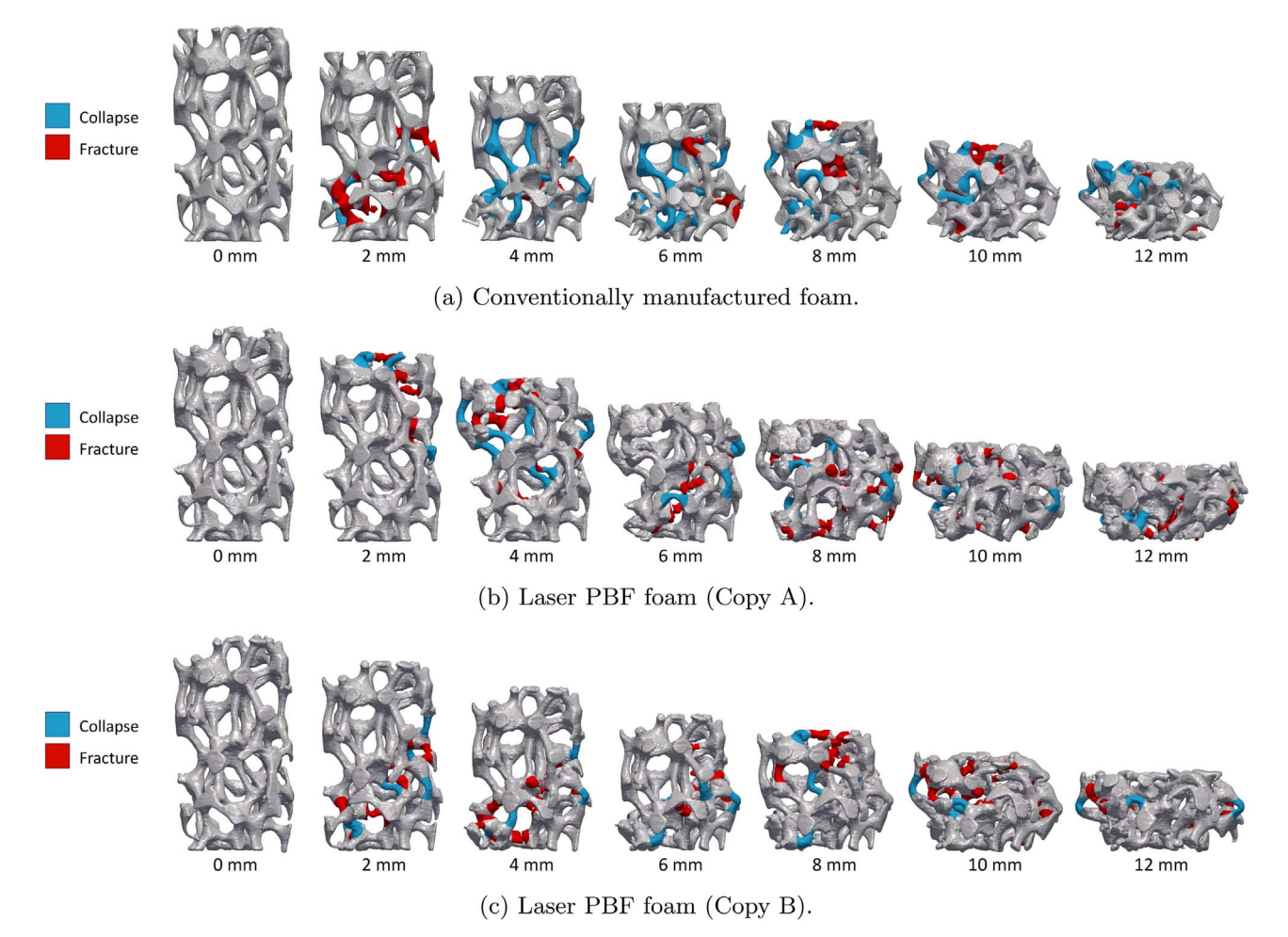


Fig. 6. X-ray computed tomography reconstructions of each foam sample imaged at 2 mm increments of displacement and color-coded according to ligament failure mechanism (collapse or fracture)

experience fracture versus collapse as the primary failure mechanism, expressed as a percentage of the total number of ligaments in each foam

Figs. 6 and 7 show the crushing progression for each foam sample imaged in 2 mm increments of applied displacement. In Fig. 6, the active regions showing signs of fracture or collapse compared to the previous displacement increment have been highlighted. In Fig. 7, regions have been highlighted to show contact among ligaments. The reconstructed and analyzed data used to generate Figs. 6 and 7 and to quantify instances of ligament failure and contact are published in a corresponding *Data in Brief* article [26].

4. Discussion

4.1. Microstructural (grain-scale) features

The orientation imaging micrographs for the ligament cross section shown in Fig. 3 were analyzed after first partitioning all points with a confidence index greater than 0.15. Based on a grain boundary misorientation threshold of 10° , there are 2436 grains (average grain diameter of 27 μm) within the ligament of the laser PBF sample and only 59 grains (average grain diameter of 194 μm) within the corresponding ligament of the investment-cast sample. There are a significant number of low-angle grain boundaries (LAGB) between 2° and 10° misorientation in the laser PBF foam compared to the investment-cast foam.

Among all boundaries with misorientations exceeding 2°, 71.7% of the total boundary length is considered to be LAGB in the laser PBF foam; whereas, only 1.4% is considered to be LAGB in the investment-cast foam. The orientation imaging microscopy data were also used to extract twin information for each sample (see [27] for details on the calculation procedure). Fig. 8 shows the parent and daughter grains identified to be recrystallization twins (Σ 3 twin boundary) based on a 5° angular tolerance between twin planes. Various twinning metrics are summarized in Table 3 for both types of foam. "Twin fraction" is defined as the area sum of all twins divided by the area sum of all grains, and "area fraction of twinned grains" is defined as the area sum of all twins and their parents divided by the area sum of all grains. While twins are not generally present in aluminum due to the high stacking fault energy, the rapid solidification process that takes place during laser-based additive manufacturing appears to induce non-negligible twinning in the aluminum alloy studied here. Notably, the area fraction of twinned grains is nearly 30% in the laser PBF foam ligament, which is an order of magnitude greater than that in the conventional foam ligament. Work by Levi and Mehrabian [28] showed that rapid solidification of aluminum leading to increased undercooling prior to nucleation can cause higher liquid/solid interface velocities and promote twinning. While the increased undercooling was accomplished in that work using an electrohydrodynamic atomization process [29], the authors suspect that the twinning mechanism for laser PBF could be similar. The grain-scale observations made here are later referenced to

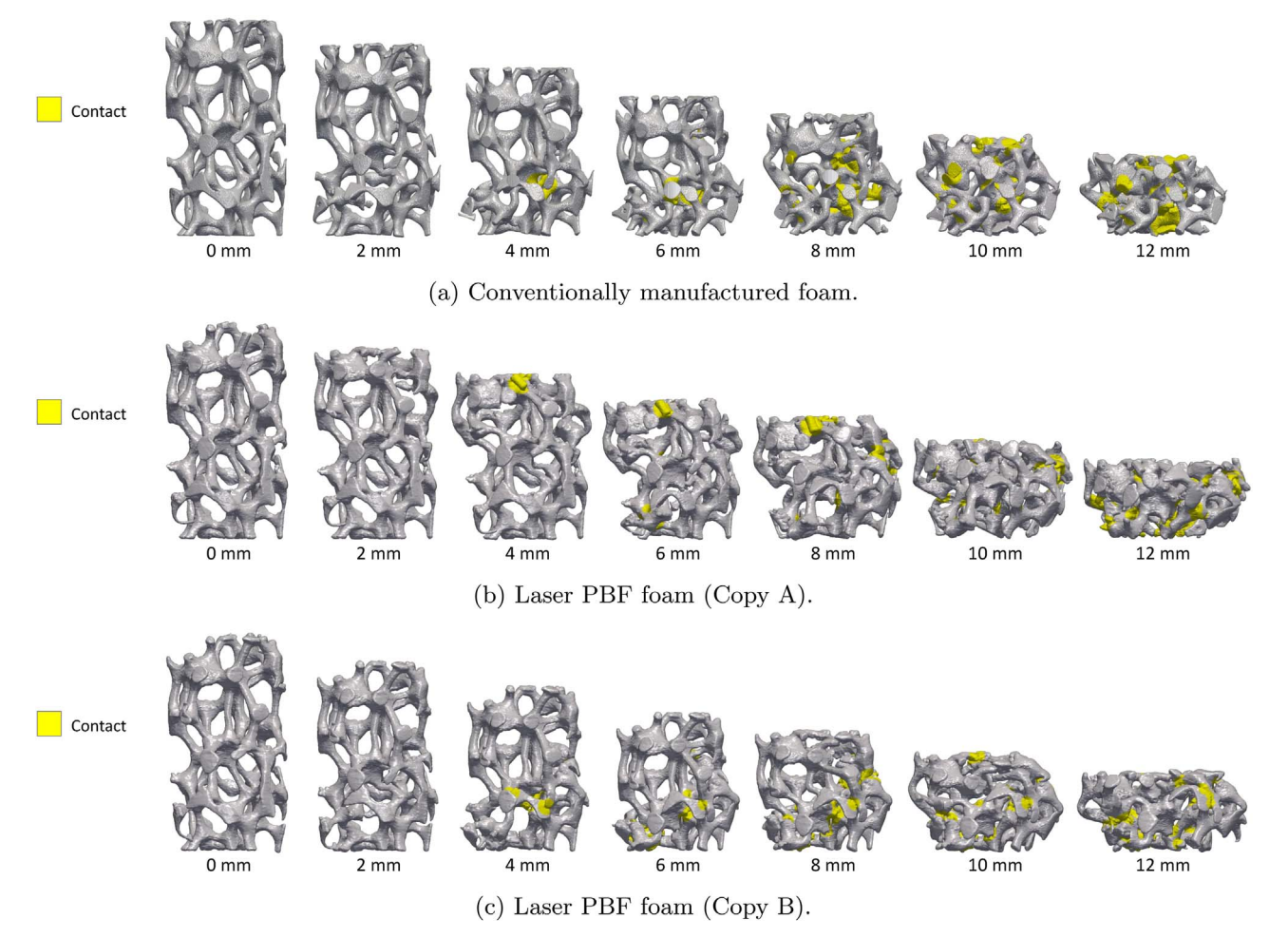


Fig. 7. X-ray computed tomography reconstructions of each foam sample imaged at 2 mm increments of displacement and color-coded according to ligament contact.

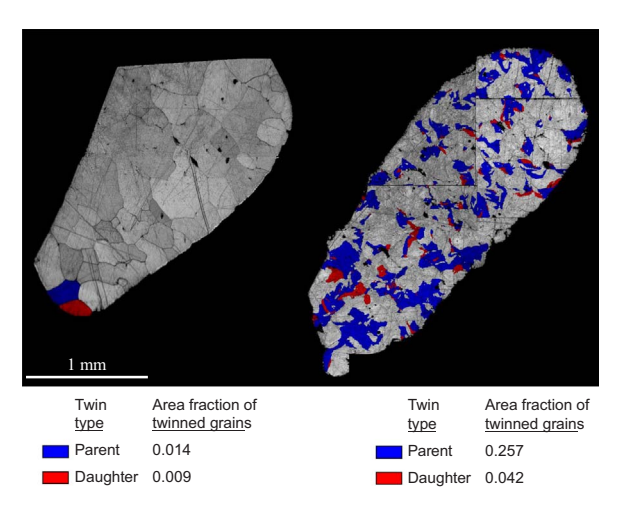


Fig. 8. Image quality map overlaid with $\Sigma 3$ twin parent/daughter map for conventional foam (left) and laser PBF foam (right).

Table 3 Statistics of FCC recrystallized twins (Σ 3) for the ligament shown in Fig. 3.

	Twin fraction	Area fraction of twinned grains	Fraction of twinned grains
Conventional foam	0.009	0.023	0.017
Laser PBF foam	0.042	0.299	0.038

explain differences in the local micromechanical behavior of the conventional and laser PBF foams.

4.2. Global mechanical behavior

As shown in the crushing response of the investment-cast and two AM foams (Fig. 4), each of the foams exhibits three general characteristics in global mechanical behavior: elastic loading, followed by softening, followed by hardening. Similar crushing characteristics of open-cell foams have been described previously by others, including Kyriakides and collaborators [30,31]. The initial stiffness of the foam (slope of the elastic loading portion) is similar for the two AM foams, but is slightly larger for the investment-cast foam. This could be due to the slight differences in the post-process heat treatments applied for the investment-cast and AM foams. The apparent softening region is caused by localized failure of individual ligaments. The investment-cast foam exhibits a more pronounced softening effect compared to the two AM copies. As the material densifies and neighboring ligaments begin contacting one another, each foam regains load-carrying capacity and exhibits the apparent hardening behavior, represented by the nominal increase in effective stress. Over the 12 mm of global displacement, Copy A of the AM foam had the largest amount of energy absorption, followed by the investment-cast foam, followed by Copy B of the AM

It is reasonable to postulate that the differences in global mechanical response were caused by variation in the evolution of damage among the three samples. Specifically, these differences are due to variations in the sequence of failure as well as differences in failure modes among corresponding localized regions of the three different

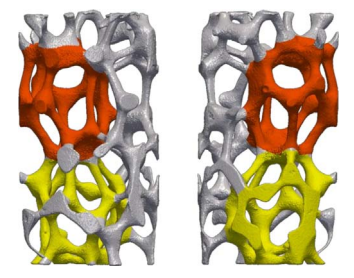


Fig. 9. Two dominant cells that appear in all three foam geometries, shown from two different reference frames. Upper cell and lower cells are called out in red and yellow, respectively. (For interpretation of the references to color in this figure legend, the reader is referred to the web version of this article.)

foams. To investigate this, the authors have attempted to correlate the different force versus displacement characteristics with the reconstructed X-ray CT data, described next.

4.3. Local mechanical behavior

Localized fracture or ligament collapse in all three foams tends to induce load shedding to neighboring ligaments, leading to the formation of macroscopically observable shear bands similar to those observed by Santorinaios et al. in non-stochastic foams [13]. These bands can be observed in Fig. 6 by the regions highlighted in red and blue. The evolution of these shear bands in the investment cast foam is closely mirrored by the shear bands in Copy B of the AM foam.

It is worth noting from Fig. 5 that the number of ligaments to remain intact was approximately the same for all three foam specimens, indicating that there is not a strong dependence of the propensity for ligament failure on the manufacturing method. Rather, the manufacturing method has a strong influence on the type of ligament failure

mechanism.

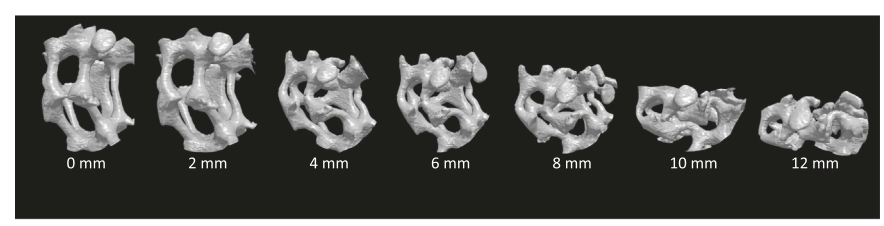
In the foam geometry, there appear to be two dominant structural cells that provide most of the load-carrying capacity (shown in Fig. 9). In order to aid the reader, each cell has been visualized separately from the rest of the foam at each stage of compression in Figs. 10 and 11. By comparing the timing of failure of these cells to the global mechanical response, it is possible to roughly explain the characteristic shape of the compressive-response curve for each of the foams. For example, the lower of the two cells is the first feature to crush in both the investmentcast foam and in AM Copy B, causing both foams to exhibit softening between 0.85 and 0.9 mm of displacement. On the other hand, that cell remained intact in Copy A of the AM foam for at least the first 2 mm of applied displacement, which is why its compressive response remains comparatively steady and increasing. In AM Copy A, the first features to collapse were the orphan ligaments, i.e. ligaments protruding from the top end of the foam that were not part of a complete cell. It is not until after 2 mm of applied displacement that the two structural cells exhibited signs of collapse in Copy A. The complete sequence of major failure events is superimposed over the global mechanical response for each of the three foams in Figs. 12-14.

The investment-cast foam exhibited a more ductile response than either of the AM copies, which were comparatively more brittle. From a microstructural standpoint, the increased ductility in the investment-cast foam can be rationalized by the significantly larger grain sizes and therefore lower density of grain boundaries per ligament, as shown in the inverse pole figure maps of Fig. 3. Consistent with these observations of global response and grain structure, the X-ray CT reconstructions from the in-situ tests reveal that the ligaments in the investment-cast foam tended to deform plastically, with fewer ligaments fracturing compared to the AM foam, as shown in Table 2. The investment-cast foam did have two major and abrupt fracture events that occurred between 8 and 10 mm of global applied displacement (see Fig. 12). The authors postulate that the reason these two fracture events were more dramatic in the investment-cast foam compared to the relatively brittle

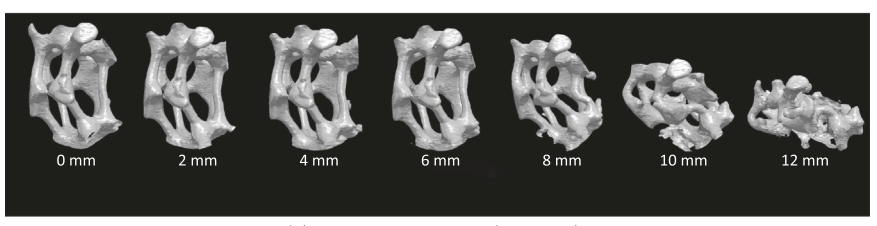
0 mm 2 mm 4 mm 6 mm 8 mm 10 mm 12 mm

Fig. 10. Progression of ligament failure within the upper cell captured at 2 mm increments of displacement.

(a) Conventionally manufactured foam.



(b) Laser PBF foam (Copy A).



(c) Laser PBF foam (Copy B).

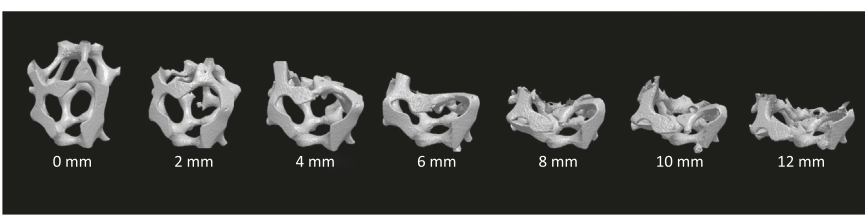
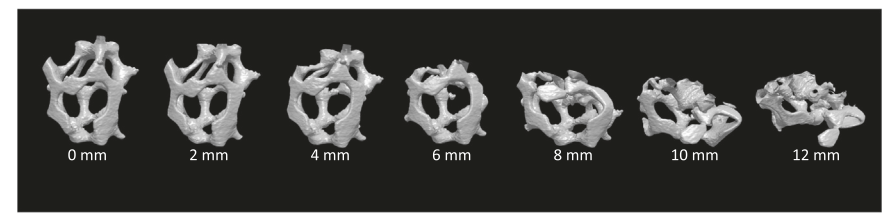
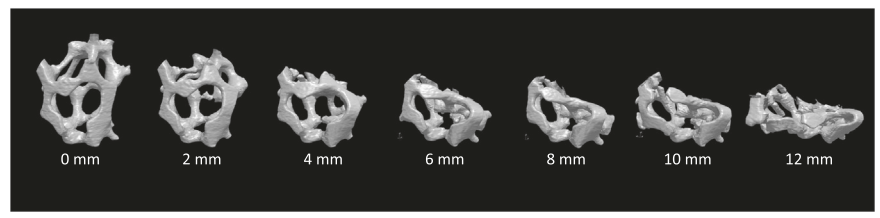


Fig. 11. Progression of ligament failure within the lower cell captured at $2\,\mathrm{mm}$ increments of displacement.

(a) Conventionally manufactured foam.



(b) Laser PBF foam (Copy A).



(c) Laser PBF foam (Copy B).

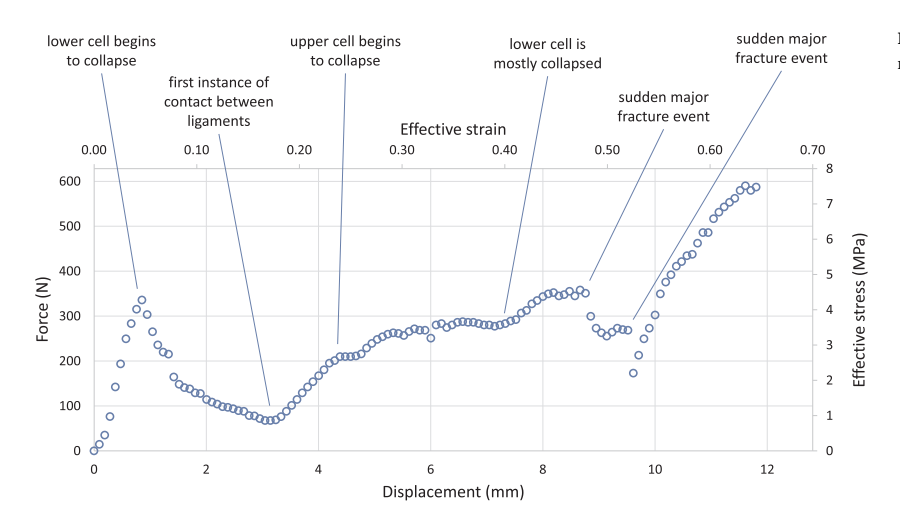


Fig. 12. Sequence of local failure events superimposed on the global mechanical response of the conventional (investment-cast) foam.

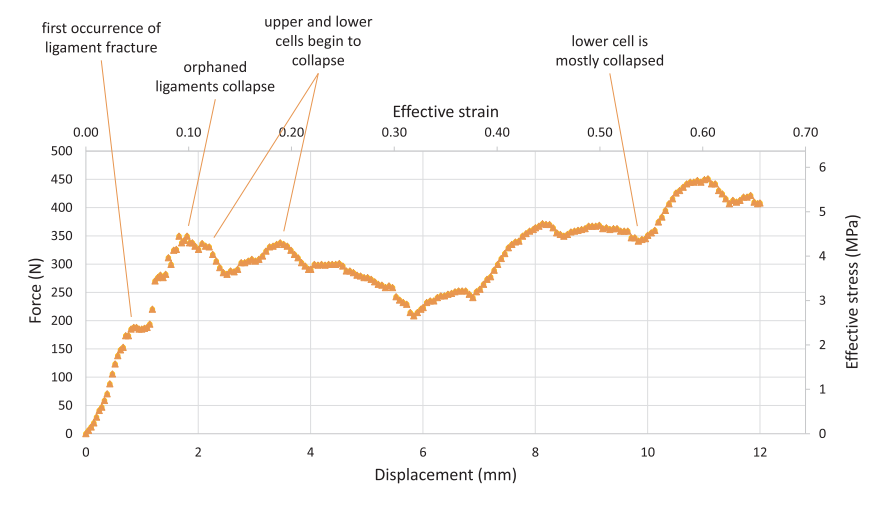


Fig. 13. Sequence of local failure events superimposed on the global mechanical response of laser PBF foam (Copy A).

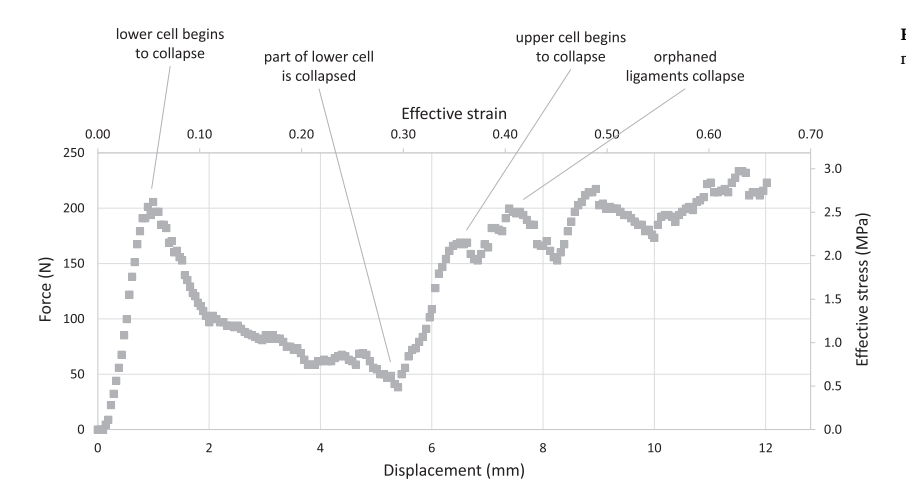


Fig. 14. Sequence of local failure events superimposed on the global mechanical response of laser PBF foam (Copy B).

Intact Ligaments	Fractured Ligaments
SO	

Fig. 15. A characteristic fracture behavior shown in different regions of laser PBF foam (Copy A).

AM foams is because the investment-cast foam is able to store more elastic strain energy than either of the AM replica foams. When two of the ligaments failed due to fracture, a large amount of strain energy was also released, and the reaction force dropped significantly. As shown in Fig. 5, the two AM foams experienced more instances of fracture than the investment cast foam, but they were less dramatic and, on average, did not appear to release as much energy per fracture event. This is also why the two AM foams had more jagged effective stress-strain curves (Figs. 13 and 14). That is, there were more fracture events, which caused the curves to repeatedly rise and fall.

Others have reported on the brittle nature of AM metals, especially aluminum [21,32,33]. Work by Louvis et al. [32] showed that such brittle behavior of laser PBF aluminum is likely attributed to thin oxide layers that form on both the solid and molten regions during the build process when oxygen is present within the build chamber. Oxides that

remain intact during the build can lead to unintended porosity and can serve to embrittle the material. The more brittle nature of the AM foams is apparent from the higher frequency of fractured ligaments compared to the investment-cast foam. An interesting fracture characteristic was observed in the laser PBF foams that was not observed in the investment-cast foam. Fig. 15 provides representative examples of this characteristic behavior captured before and after fracturing. The characteristic behavior can be recognized by the development of two distinct cracks on opposite sides of a ligament. Based on the in-situ observations, the authors believe that this characteristic fracture behavior is caused by relative lateral movement of two neighboring nodes. This relative lateral movement induces double curvature in the ligament, causing the formation of two cracks in regions of elevated tensile stresses (mode I cracks) on opposite sides of the ligament. This fracture behavior is not present in the investment cast foam, as the relatively ductile ligaments appear to bend or buckle under the same loading scenario.

Note that, despite the differences described above between the investment-cast and laser PBF foams, Copy B of the laser PBF foam exhibits a rather similar sequence of deformation events as the original, investment-cast foam. This is evident from the isolated views of cell collapse shown in Figs. 10 and 11, the general shape of the global mechanical response, and the pattern of shear bands caused by local ligament failure shown in Fig. 6. This suggests that it is possible (at least on this relatively small scale), to reproduce qualitatively similar behavior of stochastic, open-cell, investment-cast foam using laser PBF. However, the differences between Copy A and Copy B also suggest that the laser PBF process can lead to significant variability among parts, even for identical build parameters and processing conditions. This variability suggests that repeatability of parts produced by laser PBF remains an outstanding issue to address. More studies should be carried out in the future to generate statistically significant measurements of repeatability and to identify and mitigate sources of variability caused by the laser PBF process.

5. Conclusions

Grain structure, global mechanical response, and evolution of local failure mechanisms were compared among conventionally manufactured (investment cast) open-cell aluminum foam and copies produced using additive manufacturing. The copies were created by first scanning the original foam sample using X-ray computed tomography, then using the resulting STL file to reproduce the geometry of the foam using laser powder bed fusion (PBF). Care was taken to create the

copies using the same aluminum alloy as that used in the conventionally manufactured foam. Foam samples were then crushed to 66% of the initial height and imaged incrementally in-situ using X-ray computed tomography. The resulting three-dimensional reconstructions were analyzed in detail to identify onset of local collapse, fracture, and ligament contact, which were then correlated with specific regions in the global mechanical response of each foam. From this detailed study, the following conclusions can be made:

- Of two copies produced via laser PBF, one copy exhibited a similar sequence of local failure events and, correspondingly, qualitatively similar load-displacement response as the conventionally manufactured foam sample, suggesting that laser PBF is capable of producing foams that provide similar mechanical response as conventional open-cell metallic foams.
- Despite the above observation, a second laser PBF copy (which was produced at the same time and under identical conditions as the above-mentioned copy) exhibited dramatically different sequence of local failure events and, correspondingly, different load-displacement response compared to the other two foam samples, suggesting that the laser PBF process can lead to variability among parts despite being otherwise identical. More work must be done in the future to quantify both variability and repeatability with statistical significance, which is beyond the scope of this work.
- By the end of the crushing experiments, the conventional and laser PBF foam samples exhibited approximately the same percentage of ligaments that had remained intact (30–35%) versus those that had failed (65–70%). However, both laser PBF copies had 1.5–1.6 times more ligaments that eventually fractured compared to the conventional foam; whereas, the conventional foam had far more instances of ligament collapse without fracturing compared to the laser PBF

- foams. This suggests that the foams produced via laser PBF are more brittle than the original foam, which is consistent with observations in the literature [21,32,33] of additively manufactured aluminum alloys.
- Finally, as expected, the grain structure of the foam produced via laser PBF is significantly different than that of the investment-cast foam. Compared to the investment-cast foam, the laser PBF foam has an average grain size that is an order of magnitude smaller, along with a non-negligible occurrence of twins likely caused by rapid solidification. From a microstructural standpoint, the significantly larger grain sizes (and therefore fewer grain boundaries per ligament) in the investment-cast foam could explain the more dramatic softening behavior manifested in the global load-displacement response of the foam compared to that of the laser PBF foam.

Acknowledgements

Gratitude is expressed to Dr. Michael Czabaj of the Utah Composites Laboratory for providing in-kind use of the Varian X-ray CT system. This material is based upon work supported by the National Science Foundation (DMREF-1629660), and by funding from the Undergraduate Research Opportunities Program (UROP) at the University of Utah awarded to Kory Cross. This work was performed in part at the Utah Nanofab sponsored by the College of Engineering, Office of the Vice President for Research, and the Utah Science Technology and Research (USTAR) initiative of the State of Utah. The authors appreciate the support of the staff and facilities that made this work possible, including Dr. Paulo Perez. The authors also acknowledge Dr. Anthony Rollett for valuable discussions that influenced portions of the data analysis described in the manuscript.

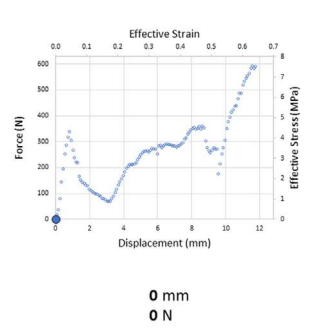
Appendix A. Supplementary material

The following are the supplementary data to this article: Video S1





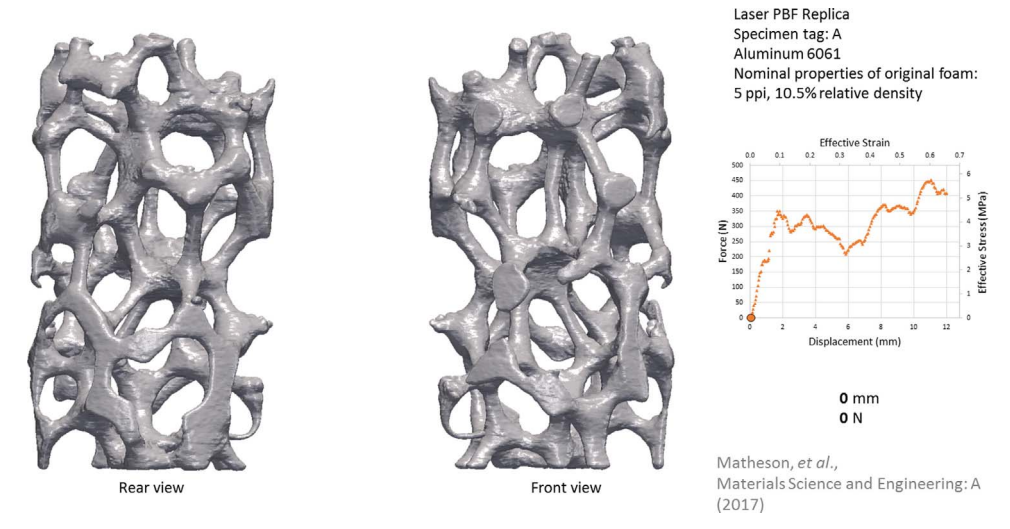
Conventionally Manufactured Foam Aluminum 6061-T6 Nominal properties of original foam: 5 ppi, 10.5% relative density



Matheson, et al., Materials Science and Engineering: A (2017)

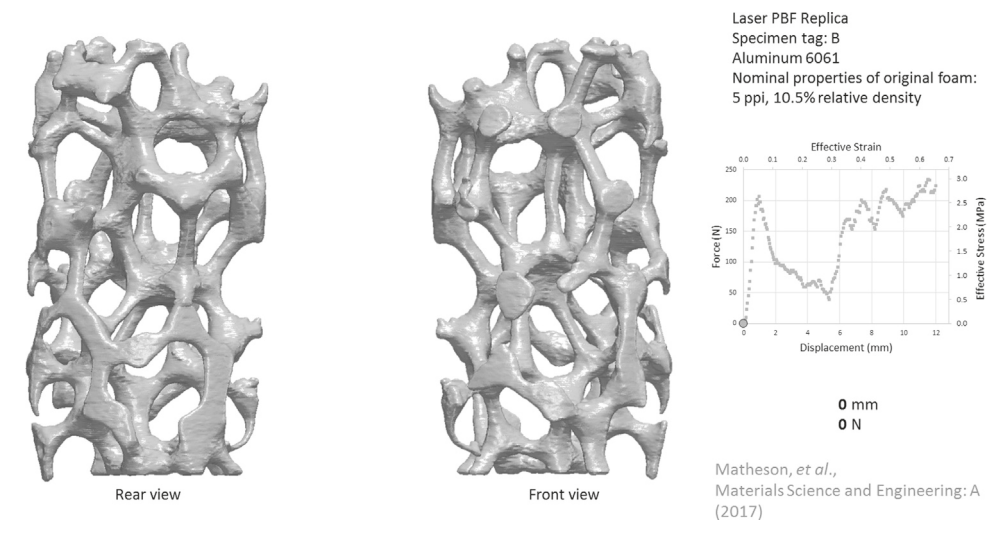
Video S1. An animation of the conventionally manufactured foam being crushed based on reconstructed CT data, alongside the current location on the force versus displacement curve. A video clip is available online. Supplementary material related to this article can be found online at http://dx.doi.org/10.1016/j.msea.2017.08.102.

Video S2



Video S2. An animation of the laser PBF foam (copy A) being crushed based on reconstructed CT data, alongside the current location on the force versus displacement curve. A video clip is available online. Supplementary material related to this article can be found online at http://dx.doi.org/10.1016/j.msea.2017.08.102.

Video S3



Video S3. An animation of the laser PBF foam (copy B) being crushed based on reconstructed CT data, alongside the current location on the force versus displacement curve. A video clip is available online. Supplementary material related to this article can be found online at http://dx.doi.org/10.1016/j.msea.2017.08.102.

References

- L.J. Gibson, M.F. Ashby, Cellular Solids: Structure and Properties, Cambridge University Press, 1999.
- [2] A.G. Evans, J. Hutchinson, M. Ashby, Multifunctionality of cellular metal systems, Progress. Mater. Sci. 43 (3) (1998) 171–221.
- [3] J. Banhart, Aluminum foams: on the road to real applications, Mrs Bull. 28 (04) (2003) 290–295.
- [4] C.-Y. Zhao, W. Lu, Y. Tian, Heat transfer enhancement for thermal energy storage using metal foams embedded within phase change materials (pcms), Sol. Energy 84 (8) (2010) 1402–1412.
- [5] R. Singh, P. Lee, R. Dashwood, T. Lindley, Titanium foams for biomedical applications: a review, Mater. Technol. 25 (3–4) (2010) 127–136.
- [6] G. Davies, S. Zhen, Metallic foams: their production, properties and applications, J. Mater. Sci. 18 (7) (1983) 1899–1911.
- [7] J. Banhart, J. Baumeister, Production methods for metallic foams, in: MRS Proceedings, vol. 521, Cambridge University Press, 1998, p. 121.
- [8] M.F. Ashby, T. Evans, N.A. Fleck, J. Hutchinson, H. Wadley, L. Gibson, Metal Foams: A Design Guide, Elsevier, 2000.
- [9] J. Banhart, Manufacture, characterisation and application of cellular metals and metal foams, Progress. Mater. Sci. 46 (6) (2001) 559–632.

- [10] H.N. Wadley, Cellular metals manufacturing, Adv. Eng. Mater. 4 (10) (2002) 726–733.
- [11] C. Körner, R.F. Singer, Processing of metal foams challenges and opportunities, Adv. Eng. Mater. 2 (4) (2000) 159–165.
- [12] B. Gorny, T. Niendorf, J. Lackmann, M. Thoene, T. Troester, H. Maier, In situ characterization of the deformation and failure behavior of non-stochastic porous structures processed by selective laser melting, Mater. Sci. Eng.: A 528 (27) (2011) 7962–7967.
- [13] M. Santorinaios, W. Brooks, C. Sutcliffe, R. Mines, Crush behaviour of open cellular lattice structures manufactured using selective laser melting, WIT Trans. Built Environ. 85 (2006).
- [14] P. Heinl, A. Rottmair, C. Körner, R.F. Singer, Cellular titanium by selective electron beam melting, Adv. Eng. Mater. 9 (5) (2007) 360–364.
- [15] P. Heinl, L. Müller, C. Körner, R.F. Singer, F.A. Müller, Cellular ti-6al-4v structures with interconnected macro porosity for bone implants fabricated by selective electron beam melting, Acta Biomater. 4 (5) (2008) 1536–1544.
- [16] L. Murr, S. Gaytan, F. Medina, E. Martinez, J. Martinez, D. Hernandez, B. Machado, D. Ramirez, R. Wicker, Characterization of ti-6al-4v open cellular foams fabricated by additive manufacturing using electron beam melting, Mater. Sci. Eng.: A 527 (7) (2010) 1861–1868.
- [17] L. Murr, S. Gaytan, F. Medina, H. Lopez, E. Martinez, B. Machado, D. Hernandez, L. Martinez, M. Lopez, R. Wicker, et al., Next-generation biomedical implants using

- additive manufacturing of complex, cellular and functional mesh arrays, Philos. Trans. R. Soc. Lond. A: Math. Phys. Eng. Sci. 368 (1917) (2010) 1999–2032.
- [18] D. Ramirez, L. Murr, S. Li, Y. Tian, E. Martinez, J. Martinez, B. Machado, S. Gaytan, F. Medina, R. Wicker, Open-cellular copper structures fabricated by additive manufacturing using electron beam melting, Mater. Sci. Eng.: A 528 (16) (2011) 5379–5386.
- [19] L.E. Murr, S.M. Gaytan, E. Martinez, F. Medina, R.B. Wicker, Next generation orthopaedic implants by additive manufacturing using electron beam melting, Int. J. Biomater. (2012).
- [20] L.E. Murr, S.M. Gaytan, D.A. Ramirez, E. Martinez, J. Hernandez, K.N. Amato, P.W. Shindo, F.R. Medina, R.B. Wicker, Metal fabrication by additive manufacturing using laser and electron beam melting technologies, J. Mater. Sci. Technol. 28 (1) (2012) 1–14.
- [21] D. Gu, W. Meiners, K. Wissenbach, R. Poprawe, Laser additive manufacturing of metallic components: materials, processes and mechanisms, Int. Mater. Rev. 57 (3) (2012) 133–164.
- [22] W.E. Frazier, Metal additive manufacturing: a review, J. Mater. Eng. Perform. 23 (6) (2014) 1917–1928.
- [23] A. F2792-12a, Standard Terminology for Additive Manufacturing Technologies, (Withdrawn 2015), ASTM International, West Conshohocken, PA, 2012.

- [24] L. Elam, Valimet Inspection Certificate, 2016. (unpublished).
- [25] Concept Laser Material Data Sheet for CL30AL/CL31AL.
- [26] K. Matheson, K. Cross, M. Nowell, A. Spear, Reconstructed and analyzed x-ray computed tomography data of investment-cast and additive-manufactured aluminum foam for visualizing ligament failure mechanisms and regions of contact during a compression test, Data in Brief (2017) (in press).
- [27] S. Wright, R. Larsen, Extracting twins from orientation imaging microscopy scan data, J. Microsc. 205 (3) (2002) 245–252.
- [28] C. Levi, R. Mehrabian, Microstructures of rapidly solidified aluminum alloy submicron powders, Metall. Trans. A 13 (1) (1982) 13–23.
- [29] J. Perel, J. Mahoney, P. Duwez, B. Kalensher, Rapid solidi cation processing: principles and technologies ii, in: r. Mehrabian, bh. Kear, m. Cohen (eds.), 1980.
- [30] L. Gong, S. Kyriakides, Compressive response of open cell foams Part ii: initiation and evolution of crushing, Int. J. Solids Struct. 42 (5) (2005) 1381–1399.
- [31] W.-Y. Jang, S. Kyriakides, On the crushing of aluminum open-cell foams: Part i. Experiments, Int. J. Solids Struct. 46 (3) (2009) 617–634.
- [32] E. Louvis, P. Fox, C.J. Sutcliffe, Selective laser melting of aluminium components, J. Mater. Process. Technol. 211 (2) (2011) 275–284.
- [33] T.M. Mower, M.J. Long, Mechanical behavior of additive manufactured, powderbed laser-fused materials, Mater. Sci. Eng.: A 651 (2016) 198–213.